Mechanical models of fault propagation folds and comparison to the trishear kinematic model

Néstor Cardozo[a],*, Kavi Bhalla[b], Alan T. Zehnder[b], Richard W. Allmendinger[a]

[a]*Dept. Earth and Atmospheric Sciences, Cornell University, Ithaca, NY 14853, USA*
[b]*Dept. Theoretical and Applied Mechanics, Cornell University, Ithaca, NY 14853, USA*

Abstract

Faults propagating through the Earth generate a wave of deformation ahead of their tip lines. We have modeled this process to understand the relationship between fold geometry and fault propagation. Using finite element modeling (FEM), we investigate the response of incompressible frictionless and frictional materials, and a compressible frictional material with associated flow, to vertical and dipping faults whose tip lines propagate at rates 3–3.5 times their slip rates. The fold geometries, finite strain, and velocity fields in models with incompressible materials are very similar to those produced by the trishear kinematic model, even though the latter uses a purely ad hoc linear velocity field. Furthermore, when the trishear grid search is applied to the final geometry of the mechanical folds, the best fit kinematic models have approximately the same propagation-to-slip ratio as was used in the FEM experiments. However, when the compressible frictional material is used, the mechanical models exhibit a main triangular shear band in front of the tip line and a conjugate shear band in the fold backlimb, both migrating with the propagating tip line. The conjugate shear band, antithetic to the fault, produces a gentle anticlinal back limb, even though there is not a bend in the fault. © 2002 Elsevier Science Ltd. All rights reserved.

Keywords: Fault propagation folding; Trishear; Mechanical models

1. Introduction

As a fault propagates through the Earth, it produces a suite of structures that include macroscopic folding as well as secondary faults, fractures, minor folding, and penetrative strain. In addition to basic scientific interest, the fault propagation folds and related deformation are important for hydrocarbon exploration and the underlying blind thrusts have considerable importance in earthquake-prone regions as demonstrated by the unexpectedness of the 1994 Northridge event (Yeats and Huftile, 1995). Fault propagation and 'forced' folds have been modeled kinematically by assuming steady velocity fields (Suppe and Medwedeff, 1990; Erslev, 1991; Hardy and Ford, 1997; Zehnder and Allmendinger, 2000), or mechanically by assuming simple rheologies and loading conditions (Braun and Sambridge, 1994; Patton and Fletcher, 1995; Niño et al., 1998; Johnson and Johnson, 2001). The kinematic models relate fold geometry to fault shape and displacement, and provide a systematic framework to construct balanced cross-sections of the structures. Kinematic models, however, rely solely on idealized

velocity distributions that may or may not have mechanical validity. Mechanical models, on the other hand, do not depend on an assumed velocity distribution. By relating fold geometry to material behavior, the models provide a physically feasible velocity distribution that characterizes the folding process. Mechanical models, however, rely on the idealistic knowledge of the rock behavior and loading conditions during folding and do not explicitly model fault tip propagation. Certainly, one is compromised between the versatility of the kinematic models and the physical soundness of the mechanical models. Testing the validity of the velocity distributions of the kinematic models with mechanical simulations, might be a solution to this conundrum.

In this paper, we present 2D, large deformation, finite element simulations of faults propagating in elastoplastic frictionless and frictional materials. Our general objective is to provide more realistic mechanical models by simulating the post yield behavior of the material and by explicitly including fault tip propagation. Additionally, we wish to test the mechanical soundness of the trishear kinematic model, which is unique in also allowing fault tip propagation to be specified (Erslev, 1991; Hardy and Ford, 1997; Allmendinger, 1998). Trishear reproduces the geometry of folds

* Corresponding author. Fax: +1-607-254-4780.
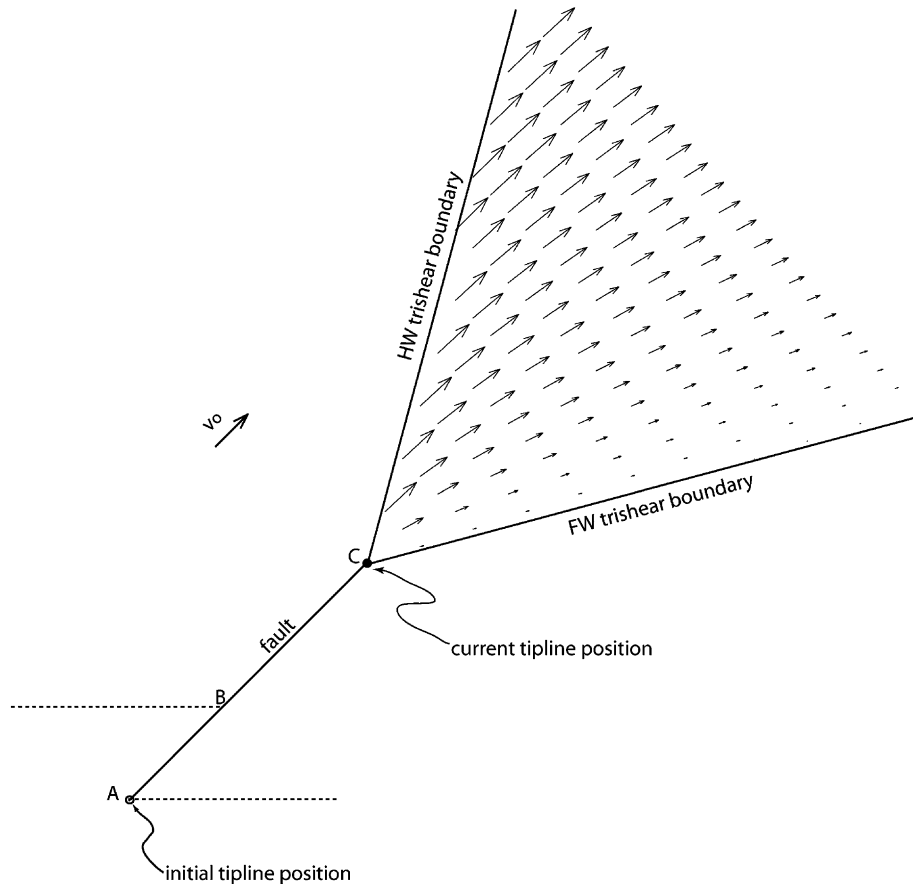 *E-mail address:* nfc3@cornell.edu (N. Cardozo).

Fig. 1. Geometry of the trishear model. Dashed horizontal lines indicate a faulted geologic marker. The slip on the fault is AB, and the fault propagates a distance AC. The propagation to slip ratio (*P/S*) is AC/AB. Velocity vectors for the simplest formulation of the model, a symmetric (with respect to the fault) triangular zone across which the component of the velocity parallel to the fault decreases linearly (Zehnder and Allmendinger, 2000).

observed in the field, predicts the finite strain distribution of analog and field examples, and allows the estimation of fault nucleation sites (Allmendinger, 1998; Allmendinger and Shaw, 2000). Trishear kinematics, however, has no mechanical basis.

Our numerical, mechanical experiments confirm the soundness of the trishear kinematic model. Vertical and inclined faults propagating in elastoplastic incompressible materials generate fold geometries, strain fields, and velocity fields similar to those of the trishear model. In the compressible frictional material, however, a conjugate shear band commonly focuses on the backlimb of the structure; the hanging wall deforms, rotates towards the fold backlimb, and uplifts. The extent and magnitude of plastic deformation in this conjugate shear band increases with material strain softening, and material dilation. Trishear replicates the geometries and the finite strain fields of folds formed in incompressible materials. Trishear, however, cannot replicate the backlimb geometries and finite strain fields of folds formed in the compressible material. The assumption of rigid hanging wall translation of trishear (and of all kinematic models) is not justified under conditions favorable to material dilation and strain softening.

2. The trishear kinematic model

Trishear (Erslev, 1991) is a kinematic model for fault propagation folds, alternative to the better-known parallel kink model (Suppe and Medwedeff, 1990). In trishear a triangular zone of distributed shear expands ahead of the propagating fault tip (Fig. 1). The hanging wall moves rigidly parallel to the fault at a velocity equal to the incremental slip (v_o) on the fault, and the footwall is fixed (Fig. 1). The rock material inside the triangular zone moves according to a velocity field that satisfies the velocity conditions at the triangle boundaries and ensures preservation of area during the deformation (Fig. 1; Hardy and Ford, 1997; Zehnder and Allmendinger, 2000). The propagation of the fault tip and the migration of the triangular zone through the rock material are explicitly specified in the model by *P/S*, the ratio of fault propagation to fault slip (Fig. 1).

Trishear deformation resembles both the geometry and the finite strain field of fault propagation folds in thick and thin skinned provinces (Erslev, 1991; Allmendinger 1998). Trishear is therefore a powerful tool to construct balanced cross-sections of fault propagation folds (Erslev, 1991; Hardy and Ford, 1997; Allmendinger, 1998), predict the distribution and orientation of fractures in the folds

(Allmendinger, 1998), and estimate the nucleation point of underlying blind thrusts (Allmendinger and Shaw, 2000).

The model, however, does not have a mechanical basis. The assumed triangular zone of distributed shear ahead of the fault tip has some analogy with the triangular zone of high shear stress in front of a mode II crack (Pollard and Segall, 1987), and the model's strain rate resembles the strain of a stationary crack in an elastic-perfectly plastic material (both are infinite as the fault tip is approached; Zehnder and Allmendinger, 2000; Rice, 1968). But even if the trishear configuration is mechanically reasonable, the assumed rigid behavior of the hanging wall, and the movement of rock material inside the triangular zone (which could be defined by an infinite number of potential velocity fields; Zehnder and Allmendinger, 2000) have not been mechanically tested. It is also not clear how the loading conditions, material mechanical behavior, and material anisotropy control the extent of the triangular zone (defined by its apical angle) and the P/S. Intuitively, the P/S might be controlled by rock competence or the surrounding effective stress (low P/S in incompetent or/and overpressured rocks; Allmendinger, 1998). Trishear fold geometries are more sensitive to P/S variations than to changes in the apical angle of the triangular zone (Allmendinger et al., 2002), but the mechanical significance of P/S and the trishear apical angle, of their magnitudes, and their relative changes is unknown.

3. Mechanical modeling of fault propagation folds

A fault propagating through the Earth imparts an irrecoverable field of deformation to the rocks immediately ahead of the fault tip (Elliott, 1976; Williams and Chapman, 1983). Fault propagation folding refers to this wave of finite deformation (Suppe, 1985). This mechanical process of simultaneous faulting and folding is characterized by three interdependent parameters: the slip on the fault, the propagation of the fault, and the internal strain of the rock material ahead of the fault tip (Williams and Chapman, 1983).

Mechanical, analytical models of fault propagation folds consider the internal deformation of the rock material in response to a displacement or velocity boundary condition that is equivalent to the slip on the fault. The models can be divided into two main groups: block motion type models, and dislocation type models. In block motion type models a displacement or velocity boundary condition is applied at the base of an incompressible, elastic (Sanford, 1959), or viscous layer (Patton and Fletcher, 1995; Johnson and Johnson, 2001). Such models are appropriate for representing the deformation of a sedimentary cover above rigid basement blocks that move along a fault (forced-folds of Stearns, 1978). In viscous rheologies, the calculated velocity fields produce geometries that resemble folds in the field and in analog experiments (Patton and Fletcher, 1995; Johnson and Johnson, 2001). Trishear-like folds form in isotropic, and kink-like parallel folds in anisotropic viscous materials (Johnson and Johnson, 2001).

Dislocation type models are more appropriate for faults that propagate through and deform rocks of similar mechanical properties. In these models a displacement boundary condition equivalent to the fault slip is applied to a crack or a fault inside a homogenous elastic media. The crack is then sealed and the residual elastic stresses and strains resulting from slippage of the fault are calculated (Manshinha and Smylie, 1971; Johnson, 2001). The computed displacement fields are similar to the ground displacements observed after earthquakes (Savage and Hastie, 1969; Chen et al., 1978), and to some extent, to the displacement fields (properly scaled) of natural and analog fault propagation folds (Rodgers and Rizer, 1981). In fact, it has been suggested that fault propagation folds result from the sum of dislocation type, elastic strain increments associated with earthquakes (King et al., 1988). However, the link between coseismic deformation and the finite strain of fault propagation folds remains enigmatic.

Although the analytical models solve for stress fields that have not reached a yielding state, it is customary to determine the orientation of potential faults by fitting Coulomb slip lines into the models' principal stress trajectories (Sanford, 1959; Rodgers and Rizer, 1981; Patton and Fletcher, 1995). The similarity of such predicted fault patterns with the orientation of secondary faulting in analog and natural fault propagation folds seems to justify this mechanically non-rational approach. Apparently, ahead of the fault tip most of the stress reorientation occurs before reaching the yielding state, and therefore the analytically computed stress fields are close in orientation (but not in magnitude) to the stress fields at the yielding state (Mandl, 1988). Analytical models, however, do not consider the intrinsic effects of faulting; mainly deformation of the rock as it moves along a frictional surface, and as the fault propagates.

Mechanical, numerical models can represent more realistically the process of fault propagation folding, albeit at the loss of some insight due to their inherent complexities. Variable material and environmental parameters, body forces, and more realistic rheologies can be included in numerical models. Finite difference and finite element methods allow the introduction of plastic, and viscous–plastic rheologies that resemble more closely the mechanical behavior of rock materials (Braun and Sambridge, 1994; Gregg Erickson and Jamison, 1995; Strayer and Hudleston, 1997; Niño et al., 1998; Smart et al., 1999). In contrast to the behavior of viscous layers (Johnson and Fletcher, 1994), material deformation in plastic rheologies is entirely dependent on the applied loading but independent of the rate of change of the load (Mandl, 1988). The absence of time in plastic deformation might seem inappropriate to characterize rock materials, but in the upper crust frictional regime where most of the deformation is accommodated by slip along fractures, it is justified (Mandl, 1988). Alternatively, one
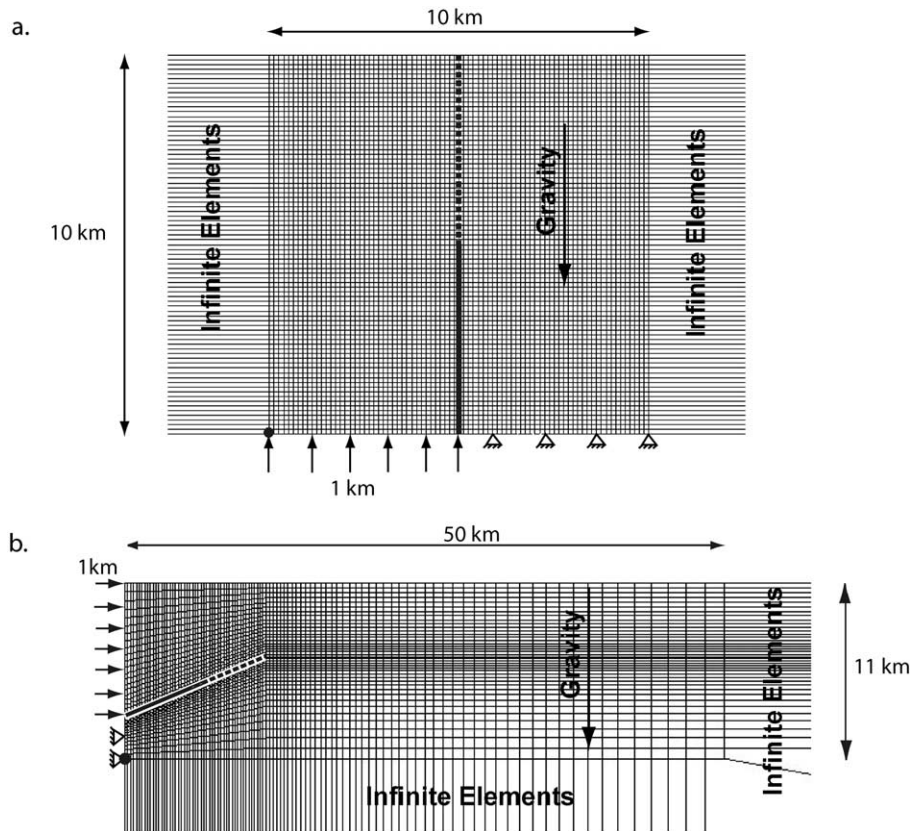
Fig. 2. Finite element meshes and boundary conditions of the numerical experiments. (a) Vertical fault. (b) Dipping fault. Heavy line indicates the initial fault surface. Dashed line indicates the bonded contact surface, or trajectory of fault propagation, which is pulled apart during deformation according to a prescribed rate of fault growth. In both experiments, the origin of coordinates is at the left corner of the finite element mesh (black dot).

can combine viscous behavior with plastic flow type models to simulate time-dependent processes without frictional slip (i.e. pressure solution creep) and time-independent frictional slip processes (i.e. cataclasis; Gregg Erickson and Jamison, 1995).

Numerical models of fault propagation folds have been implemented to investigate the simultaneous development of folding and faulting (Braun and Sambridge, 1994), the internal deformation of the rock mass as it moves along the fault (Strayer and Hudleston, 1997, their model B; Niño et al., 1998), the role of anisotropy and bed-parallel slip in the potential propagation path of a thrust fault (Niño et al., 1998), and the effect of fault friction on the internal deformation of the rock material (Smart et al., 1999). However, none of these models considers explicitly the propagation of the fault tip. In the Braun and Sambridge (1994) experiment, the fault propagates dynamically in response to crustal shortening, a basal velocity singularity, and the mechanical response of the elastoplastic material. But the propagation of the fault is denoted by a geometrical, not a mechanical discontinuity. The continuity of the rock domain is preserved throughout the experiment. In the Strayer and Hudleston (1997) and Smart et al. (1999) experiments, the fault surface (denoted by a sliding frictional surface) is specified before deformation. In the Niño et al. (1998)

experiment the fault tip remains stationary during deformation.

In this study we present numerical, mechanical experiments that thoroughly simulate the dynamic interaction of fault propagation, fault slip, and internal rock deformation. In addition to the advantages of the current numerical models for fault propagation folding, the experiments include fault propagation explicitly by specifying a mechanical discontinuity that grows during the deformation.

4. Numerical experiments

We implemented 2D, plane strain, large deformation finite element analyses of faults propagating in plastic materials using ABAQUS/Standard 5.8™, a general purpose, finite element code. This code provides well-documented elasto−plastic material models that realistically simulate rock behavior, efficiently solves nonlinear large deformation problems by incrementally applying the load, and explicitly introduces fault propagation based on a critical stress or a time-dependent failure criterion.

4.1. Model configurations and boundary conditions

We performed crustal scale experiments with two

Table 1
Summary of finite element simulations. For all models: $\rho_{\text{rock}} = 2500$ kg/m^3, $E = 30$ GPa, $\nu = 0.25$

Model	Material properties[a]	Hardening[b]	Fault dip & friction	Imposed displacement (km)	FW initial tip line[c] (km)	HW initial tip line[c] (km)	final tip line[c] (km)	P/S
Vertical fault								
Elastoplastic	200.0	0.00	90.0, 0.3	1.00	5.02, 5.03	5.04, 5.95	5.10, 8.00	3.2
Drucker–Prager[d]	40.9, 30.0, 0.0	0.00	90.0, 0.2	1.00	5.03, 5.03	5.05, 5.96	5.09, 8.03	3.2
Drucker–Prager[d]	39.8, 28.8, 39.8	0.00	90.0, 0.3	1.00	5.02, 5.04	5.03, 5.96	5.05, 8.00	3.2
Dipping fault								
Elastoplastic	200.0	0.00	45.0, 0.1	1.00	6.83, 9.81	7.76, 10.73	9.82, 12.72	3.2
Drucker–Prager[e]	40.9, 45.00, 0.0	0.00	35.0, 0.3	1.00	6.85, 7.74	7.74, 8.33	9.82, 9.79	3.3
Drucker–Prager[e]	39.8, 43.2, 39.8	0.00	22.0, 0.3	1.00	6.82, 5.74	7.70, 6.16	9.68, 7.12	3.3
Varying hardening (compressible materials)								
Drucker–Prager	39.8, 43.2, 39.8	−0.001	22.0, 0.3	1.00	6.82, 5.74	7.71, 6.16	9.66, 7.12	3.2
Drucker–Prager	39.8, 43.2, 39.8	0.001	22.0, 0.3	1.00	6.82, 5.74	7.70, 6.15	9.68, 7.12	3.3
Drucker–Prager	39.8, 43.2, 39.8	0.005	22.0, 0.3	1.00	6.83, 5.74	7.68, 6.13	9.70, 7.12	3.4
Drucker–Prager	39.8, 43.2, 39.8	0.01	22.0, 0.3	1.00	6.84, 5.74	7.66, 6.11	9.71, 7.11	3.5
Varying friction[f] (compressible materials)								
Drucker–Prager	23.9, 49.6, 23.9	0.00	30.0, 0.3	1.00	6.83, 6.92	7.69, 7.43	9.69, 8.65	3.3
Drucker–Prager	30.2, 48.0, 30.2	0.00	27.0, 0.3	1.00	6.83, 6.46	7.70, 6.93	9.68, 8.04	3.3
Drucker–Prager	39.8, 43.2, 39.8	0.00	22.0, 0.3	1.00	6.82, 5.74	7.70, 6.16	9.68, 7.12	3.3
Drucker–Prager	46.2, 37.2, 46.2	0.00	17.0, 0.3	1.00	6.81, 5.08	7.70, 5.42	9.67, 6.27	3.3

[a] For elastoplastic σ_{yld} (MPa). For Drucker–Prager β, d (MPa), ψ. Incompressible materials $\psi = 0$. Compressible materials $\psi > 0$.
[b] Hardening modulus as a fraction of Young's modulus, E.
[c] x and y coordinates. Origin of coordinates at left corner of finite element mesh. FW = footwall, HW = hanging wall.
[d] Corresponding Mohr–Coulomb friction angle and cohesion = 30°, 20 MPa.
[e] Corresponding Mohr–Coulomb friction angle and cohesion = 30°, 30 MPa.
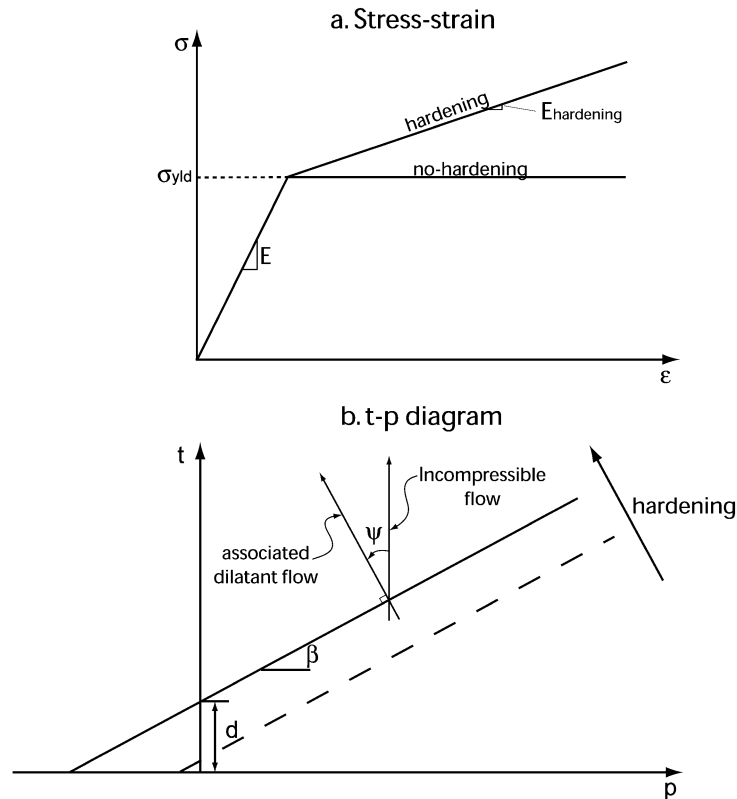[f] Corresponding Mohr–Coulomb friction angles = 15, 20, 30 and 40°. Corresponding cohesion = 30 MPa.

a. Stress-strain

b. t-p diagram

Fig. 3. Mechanical behavior of the materials used in the experiments. (a) Stress (σ) vs. strain (ϵ) behavior of elastoplastic (frictionless or frictional) materials, with and without strain hardening. σyld: yield stress, E: Young's modulus, Ehardening: hardening modulus. (b) Drucker–Prager failure model in a deviatoric stress (t) vs. mean normal stress (p) diagram. In compressible materials with an associated flow rule, the flow is perpendicular to the yield surface ($\psi = \beta$). In incompressible materials $\psi = 0$. See text for definition of additional symbols.

configurations: a vertical fault and a dipping fault (Fig. 2). In both configurations four node quadrilateral elements are used to discretize the rock domain, and infinite elements to simulate the far field behavior at the unconstrained sides of the domain. Meshes of 6400 elements with an element size of 125×125 m, and 4000 elements with an element size of 200×100 m close to the fault surface are used in the vertical and dipping fault experiments, respectively (Fig. 2). Experiments with different mesh sizes and mesh geometries yielded similar strain and velocity fields. Our observations are scale and mesh geometry independent.

In the vertical fault experiment a vertical displacement boundary condition is applied at the left base of the model, and the right base is held fixed (Fig. 2a). This configuration is similar to the geometry and the loading conditions of basement-cored uplifts limited by high angle reverse faults (Prucha et al., 1965; Stearns, 1971, 1978). In the dipping fault experiment a horizontal displacement boundary condition is applied at the left side of the hanging wall, and the left side of the footwall is held fixed (Fig. 2b). These loading

conditions are similar to those assumed in tectonic over-thrusting (Hubbert, 1951; Elliott, 1976), and in crustal short-ening models of basement-cored uplifts (Berg, 1962).

Gravity is imposed on all elements. The loading is divided into an initial static step that brings the rock mass to a lithostatic state of stress, and a second static step in which the displacement boundary conditions are applied. To simulate the fault (thick line; Fig. 2a and b), we used contact surfaces with a basic Coulomb friction model where sliding begins when the shear stress exceeds the product of the coefficient of friction and the pressure normal to the contact surfaces. To guarantee numerical convergence, we adopted low coefficients of friction in all the simulations (0.3–0.1; Table 1). These values are lower than those reported in shear tests of small specimens (0.6–0.8; Byerlee, 1978) but are within the range suggested by studies on the strength of large faults (Turcotte and Schubert, 1982; Bird and Baumgardner, 1984).

Fault propagation is simulated with bonded (joined at their nodes) contact surfaces ahead of the initial fault tip

Fig. 4. Contours of equivalent plastic strain superimposed on deformed configuration of initially horizontal markers for the vertical fault experiment with (a) frictionless, (b) incompressible Drucker–Prager, and (c) compressible Drucker–Prager materials. Broken circles indicate the initial position of the tip line of the fault (in the hanging wall and footwall). White circle indicates the final position of the tip line.

a.

	0.0
	0.1
	0.35
	0.6
	1.16

b.

	0.0
	0.1
	0.35
	0.6
	2.1

c.

	0.0
	0.1
	0.2
	0.3
	0.45
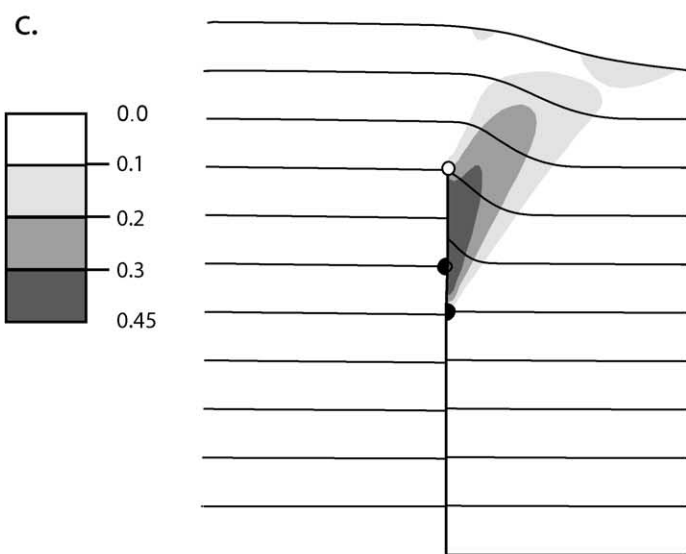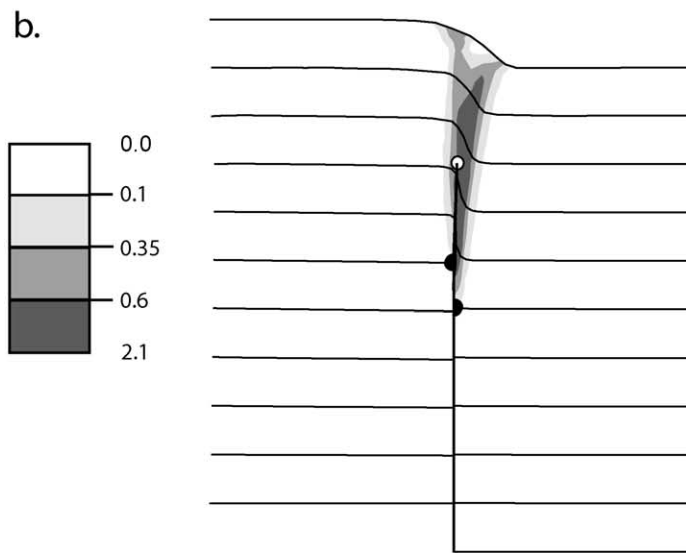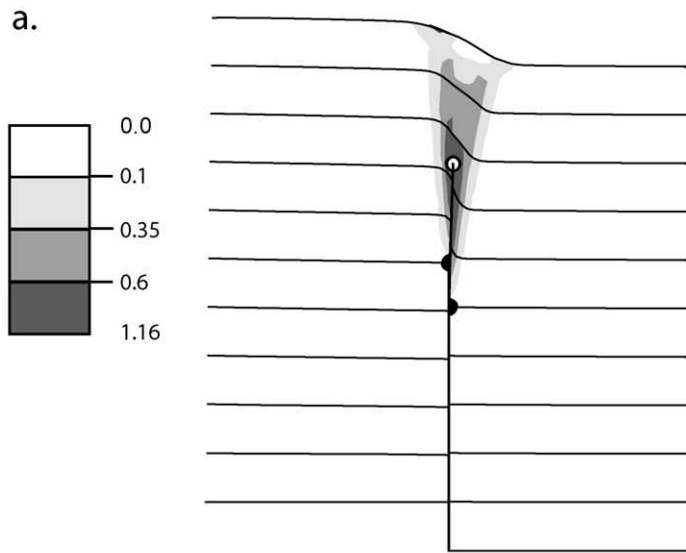
0   2 km

(dashed line; Fig. 2a and b), that during the deformation were torn apart (released at their nodes) according to a specified history of fault growth. Therefore, the trajectory and the rate of fault propagation are prescribed in the numerical simulations. In the experiments the fault propagates between 3.2 and 3.5 times the slip on the fault ($P/S = 3.2$–3.5; Table 1). These prescribed P/S ratios are within the range of values found in real fault propagation folds (Williams and Chapman, 1983; Hardy and Ford, 1997; Allmendinger, 1998).

4.2. Material properties

The mechanical behavior of the materials used in the experiments is characterized initially by an elastic response, followed by non-recoverable plastic deformation when the load exceeds some limit, 'the yield stress' (Fig. 3a). Since yielding (onset of non-recoverable deformation) occurs at a stress less than 1% the elastic modulus of the materials (Table 1), most of the deformation is dominated by plastic strains. We used materials with strain rate independent yield, and either pressure stress independent yield (frictionless), or pressure stress dependent yield (frictional). Frictionless materials are a good first approximation of brittle deformation in the upper crust (Desai and Siriwardane, 1984; Braun and Sambridge, 1994). Frictional materials, however, are necessary to reproduce the observed increase of yield stress with confining pressure in rocks (Jaeger and Cook, 1979).

A Mises yield surface with associated flow (incompressibility) was assumed for the frictionless materials. For the frictional materials we used a linear Drucker–Prager model (Fig. 3b) with a yield surface expressed by the equation (Desai and Siriwardane, 1984):

$$t = p\tan\beta + d \tag{1}$$

where p is the mean normal stress, t is a measure of the deviatoric stress, and β and d are the Drucker–Prager friction angle and cohesion, respectively. Analogous to the more familiar Mohr–Coulomb model, the linear Drucker–Prager model assumes a linear relation between the yield stress and the confining pressure (Fig. 3b). The main difference between these two frictional material models is that Mohr–Coulomb assumes that failure is independent of the value of the intermediate principal stress, while Drucker–Prager does not (Mendelson, 1968; Desai and Siriwardane, 1984). Both incompressible (dilation angle (ψ) = 0; Fig. 3b) and compressible materials with associated flow ($\psi = \beta$; Fig. 3b) were considered in the frictional materials. The second case, although not realistic (very brittle rocks typically have dilation angles of one quarter of their friction angles; Hoek, 2000), provided an end scenario to evaluate the effects of dilation on folding.

Values of the constants required for the frictionless material model (Table 1) were taken from the literature (Jaeger

and Cook, 1979; Ranalli, 1987). Values for the linear Drucker–Prager material model (Table 1) were calculated from well-documented Mohr–Coulomb parameters (Kulhawy, 1973; Jaeger and Cook, 1979; Carmichael, 1989) using the equations (Desai and Siriwardane, 1984, their equations 10-8):

$$\tan\beta = \frac{\sqrt{3}\sin\phi}{\sqrt{1 + \frac{1}{3}\sin^2\phi}} \quad \text{and} \quad \frac{d}{c} = \frac{\sqrt{3}\cos\phi}{\sqrt{1 + \frac{1}{3}\sin^2\phi}} \tag{2}$$

for $\psi = \beta$

$$\tan\beta = \sqrt{3}\sin\phi \quad \text{and} \quad \frac{d}{c} = \sqrt{3}\cos\phi \quad \text{for} \quad \psi = 0 \tag{3}$$

where ϕ and c are the corresponding Mohr–Coulomb friction angle and material cohesion. Eq. (2) is for compressible materials with associated flow, and Eq. (3) is for incompressible materials (non-associated flow). In the dipping fault simulations, the dip of the fault is controlled by the frictional properties of the material. In frictionless materials the fault dips 45° (Table 1). In Drucker–Prager materials the dip of the fault is function of the friction (β) and dilation (ψ) angles (Table 1). In the experiments, the fault trajectory bisects the generated zone of plastic strain ahead of the fault tip, which has an orientation that is also intrinsically related to the frictional properties of the material.

We studied the effects of material strain hardening or softening (increase or decrease of strength with strain) and material friction in Drucker–Prager compressible materials (Table 1). Hardening is defined by the ratio between the hardening modulus and the elastic modulus of the material (Fig. 3a and b):

$$H\text{ratio} = E\text{hardening}/E \tag{4}$$

5. Results

In this section we present the results of our mechanical simulations and compare them with the trishear kinematic model. To model the mechanical folds with trishear, we grid searched for the best inverse trishear models that restored the folded markers of the mechanical experiments to their original planar orientations (Allmendinger, 1998). We used fixed values for the trishear parameters known in the experiments—ramp angle and final tip line location—and grid searched for P/S (from 2.5 to 3.5), trishear angle (from 5 to 60°), and fault slip (from 0 to 2 km). In all cases, the grid search gave the correct P/S prescribed in the mechanical experiments. We then ran forward these best trishear models and compared their geometries, finite strain, and velocity fields with those of the mechanical experiments.

5.1. Vertical fault models

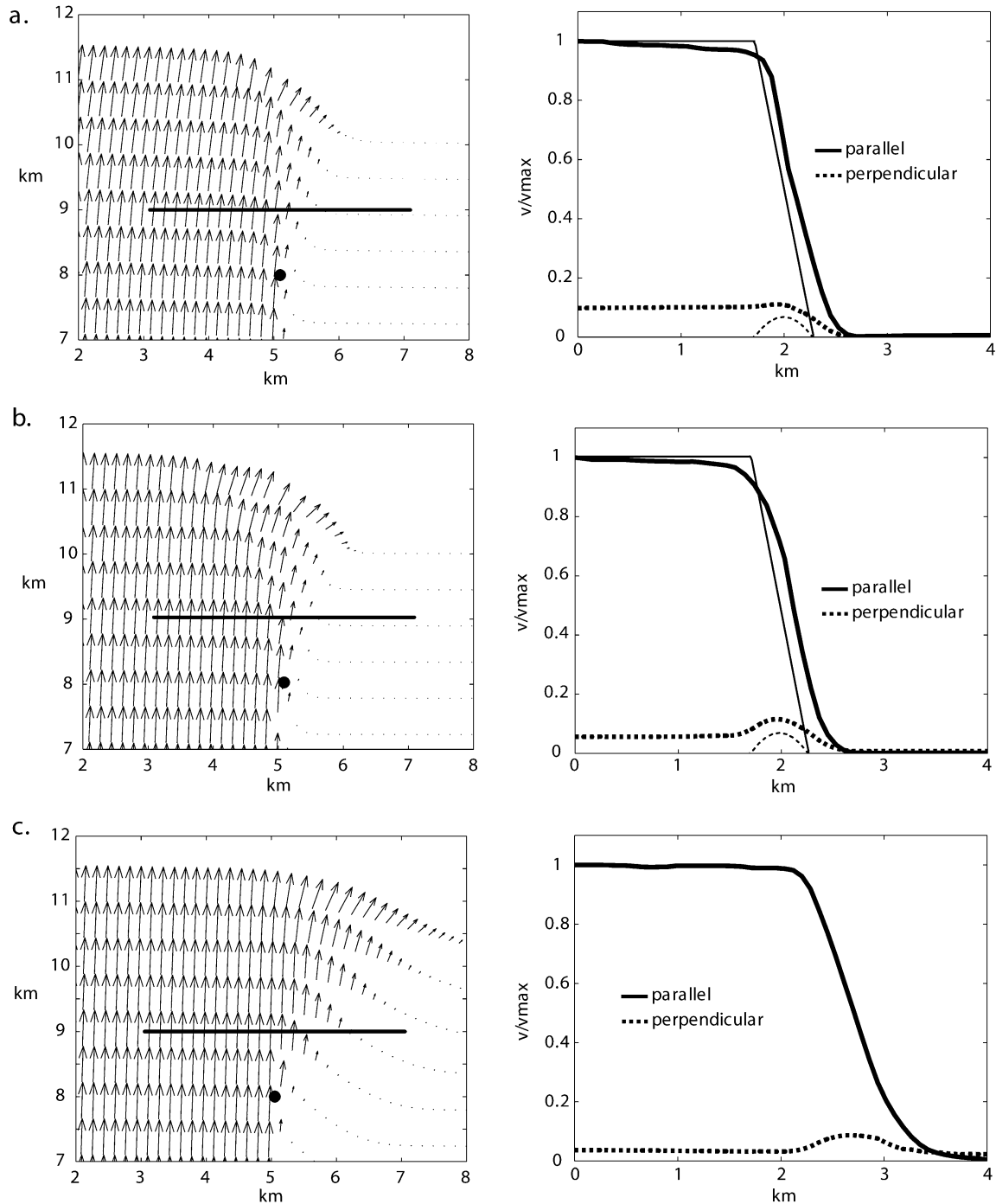Contour plots of equivalent plastic strain (Hill, 1950)

Fig. 5. Velocity field (left side) and variation of velocities parallel and perpendicular to the fault (thick lines on right side) along a tie rod (heavy line in velocity field), for the vertical fault experiment with (a) frictionless, (b) incompressible Drucker–Prager, and (c) compressible Drucker–Prager materials. Black dot in velocity field indicates the final position of the tip line. In velocity variation plot the velocities are plotted as fractions of the maximum velocity parallel to the fault (v/v_{max}). The origin of the horizontal coordinate is at the left end of the tie rod. Thinner lines denote the velocity profiles of the best-fit trishear model.

superimposed on the deformed geometry of initially horizontal markers illustrate the finite strain field of the experiments (Fig. 4). A vertical fault propagating in a frictionless (Fig. 4a) or a frictional incompressible (Fig. 4b) material generates a symmetric to slightly asymmetric (with respect to the fault) zone of plastic deformation. The magnitude of the equivalent plastic strain in this zone increases towards

the fault tip (Fig. 4a and b). The resultant folds have forelimbs that taper from steeper dip angles near the fault tip to gentler dip angles at the surface (Fig. 4a and b). Fold tightness and thinning of the marker horizons increases towards the fault tip (Fig. 4a and b). The forelimb dips are steeper and the fold width is less in the frictional incompressible (Fig. 4b) than in the frictionless material (Fig. 4a). The final
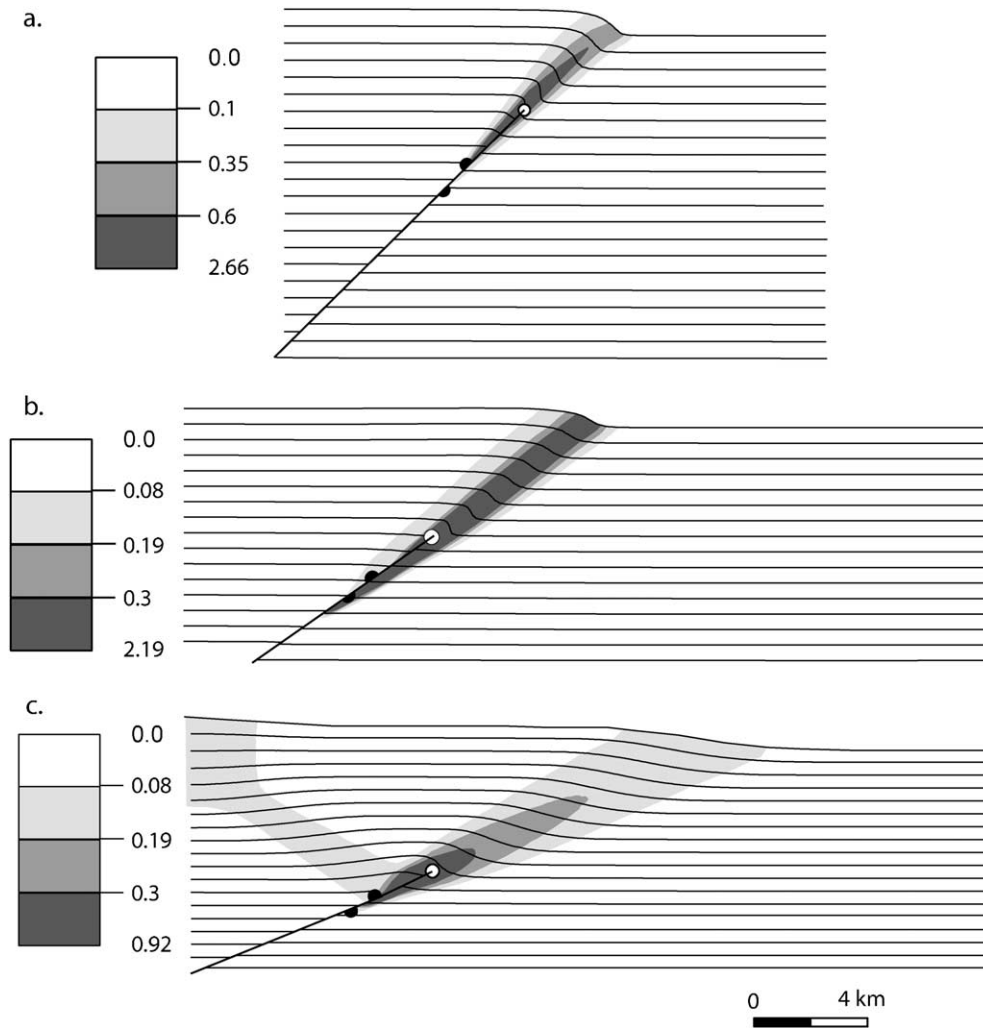
Fig. 6. Contours of equivalent plastic strain superimposed on deformed configuration of initially horizontal markers for the dipping fault experiment with (a) frictionless, (b) incompressible Drucker–Prager, and (c) compressible Drucker–Prager materials.

fold geometries resemble the drape folds of the Rocky Mountain foreland (Prucha et al., 1965; Stearns, 1971; Livesey, 1985, his seismic line B).

A vertical fault propagating in the frictional compressible material produces a finite strain field that differs from the above two cases (Fig. 4c). The fault generates a zone of plastic strain in its footwall (Fig. 4c). This strain localization is explained by the fact that under the applied displacement boundary conditions the material in the footwall is in tension. The yield stress, which is pressure dependent, is much lower and therefore the material yields at these localities. This produces material dilation and a decrease in the confining pressure, which in turn promotes further yielding. In a more realistic model in which the trajectory of fault propagation was entirely controlled by the physics of the material (and not prescribed before the experiment), there would be steep reverse and upwards-convex faults emanating from the vertical fault towards the plastic strain zone. These faults have been documented in sandbox experiments (Mandl, 1988, his figures I.2-71 and II.7-33), and in base-

ment uplift structures of the Wyoming foreland (upthrust of Prucha et al., 1965).

Velocity fields calculated by subtracting the displacements at the end and at 99% the total time of the experiments illustrate the kinematics of the deformation (left side; Fig. 5). In the simulations, the velocity vectors are subparallel to the fault in the hanging wall and decrease in magnitude and vary in direction across a triangular zone (with apex at the fault tip) symmetric (left side; Fig. 5a and b) or asymmetric (left side; Fig. 5c) to the fault. Profiles of the velocities parallel and perpendicular to the fault (thick lines on right side; Fig. 5) along a tie rod perpendicular to the fault, and 1000 m ahead of the fault tip (heavy line on left side; Fig. 5) depict the variation of velocity across this zone. In frictionless and frictional incompressible materials the velocity parallel to the fault decreases almost linearly (thick continuous line on right side; Fig. 5a and b). The velocity perpendicular to the fault has a parabolic variation, with a maximum at the bisector of the triangular zone (thick dashed line on right side; Fig. 5a and b). These velocity
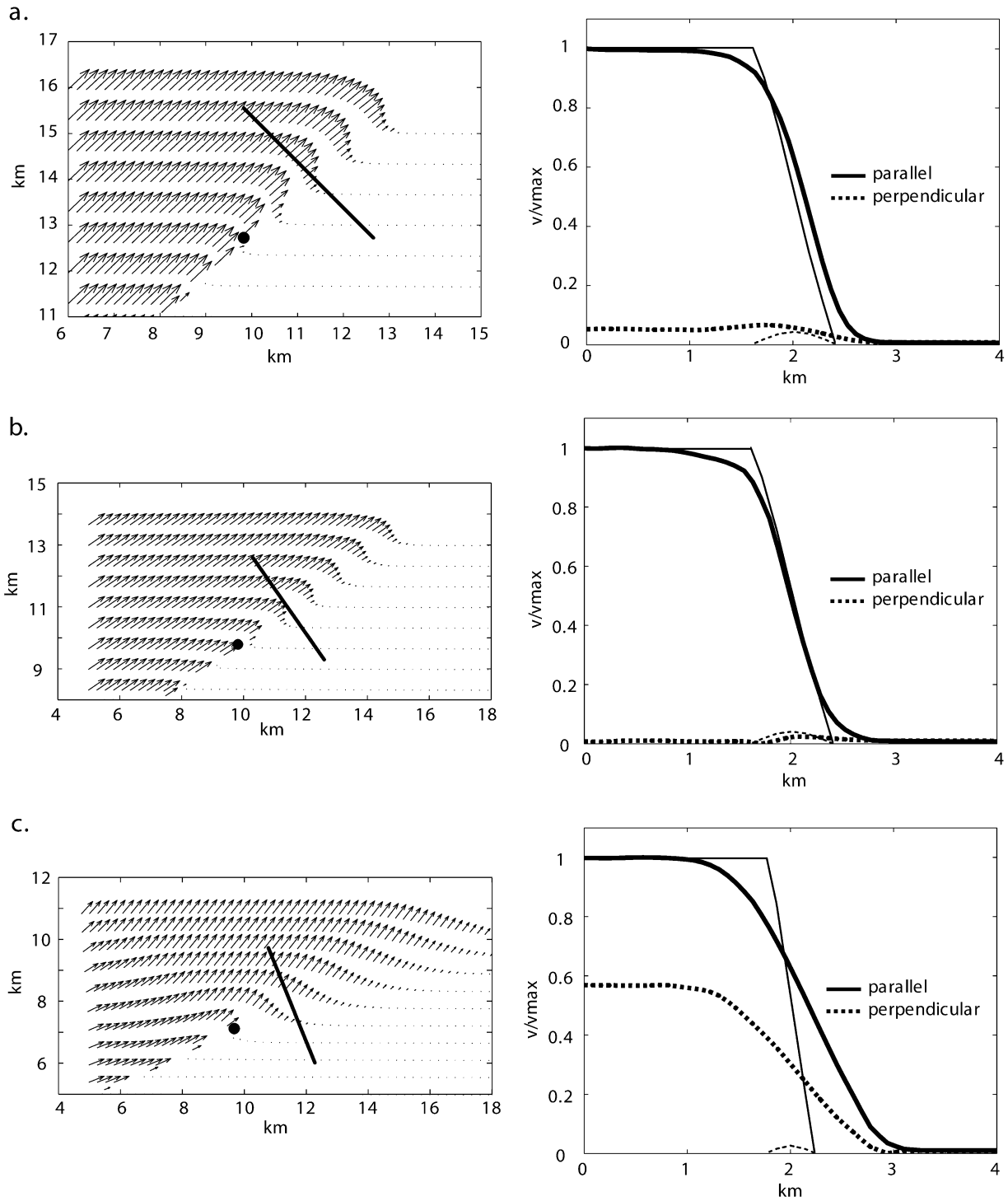
Fig. 7. Velocity field (left side) and variation of velocities parallel and perpendicular to the fault (thick lines on right side) along a tie rod (heavy line in velocity field), for the dipping fault experiment with (a) frictionless, (b) incompressible Drucker–Prager, and (c) compressible Drucker–Prager materials. Black dot in velocity field indicates the final position of the tip line. Thinner lines in velocity profiles denote the velocity variation of the best-fit trishear model.

profiles are strikingly similar to those of a symmetric, linear trishear zone (Hardy and Ford, 1997; Zehnder and Allmendinger, 2000). In fact, the velocity profiles of the best-fit trishear models (thin lines on right side; Fig. 5a and b) for the fold geometries of the experiments (Fig. 4a and b); are close to the velocity profiles of the mechanical experiments

(thick lines on right side; Fig. 5a and b). However, there is a subtle difference with respect to the trishear model. The velocity perpendicular to the fault in the hanging wall material outside the triangular zone is non-zero (thick dashed line from 0 to 2 km on right side; Fig. 5a and b). Contrary to trishear (and to all kinematic models), the hanging wall does
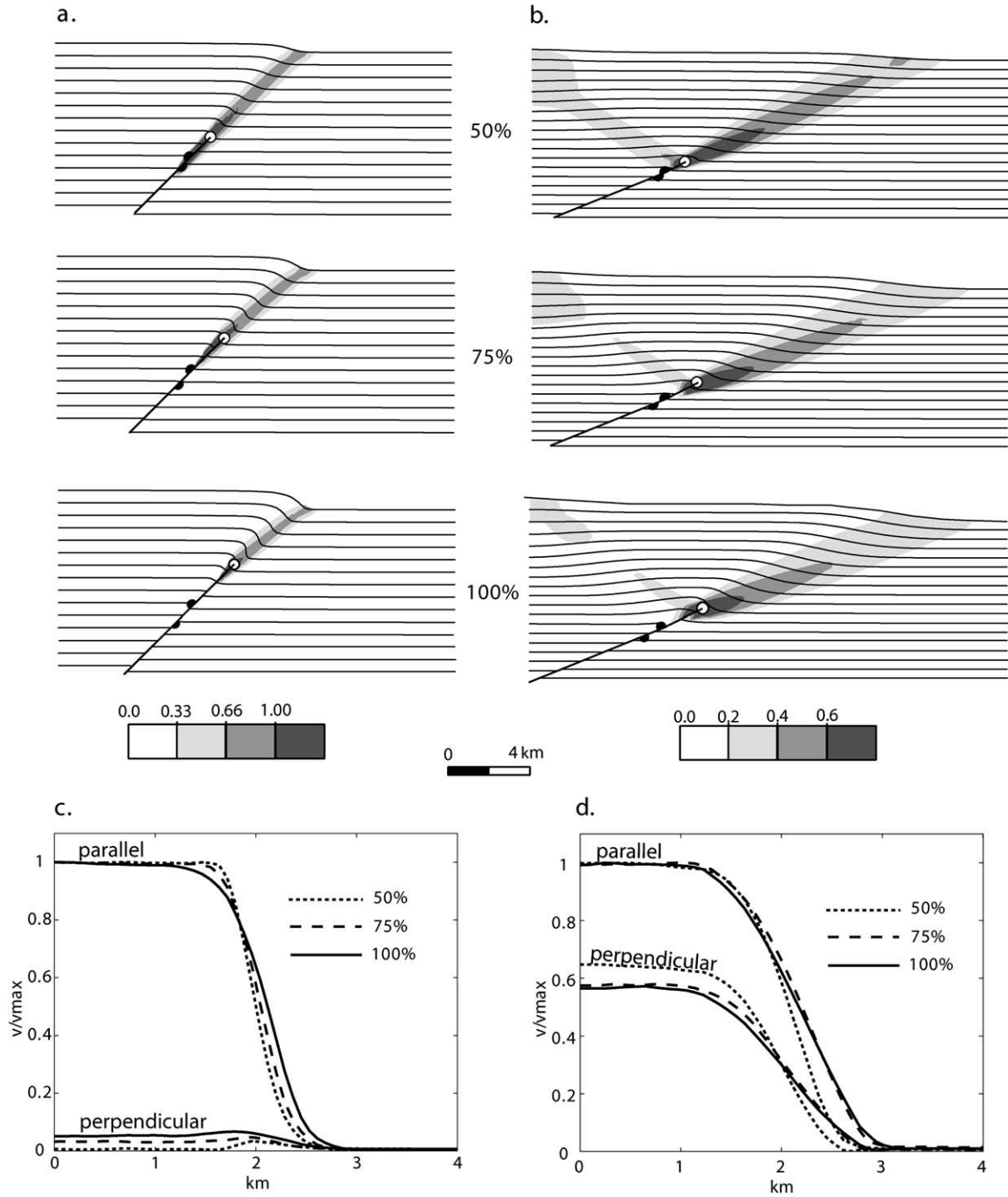
Fig. 8. Evolution of the dipping fault experiment in (a) and (c) frictionless or (b) and (d) compressible Drucker–Prager materials. In (a) and (b) the experiment evolution is depicted by contours of maximum principal strain rate superimposed on the deformed marker configuration at 50, 75 and 100% the total time of the experiment. In (c) and (d) the evolution is displayed by profiles of the velocities parallel and perpendicular to the fault along a tie rod perpendicular to the fault and 2000 m in front of the fault tip at times 50, 75, and 100% the total time of the experiment.

not move rigidly parallel to the fault, but deforms internally and moves oblique to the fault before entering the triangular zone of velocity variation. In the frictional compressible material the velocity profiles (right side; Fig. 5c) are some-what similar to those of incompressible materials (right side; Fig. 5a and b). Nonetheless, the velocity vectors vary over a

much broader zone, asymmetric with respect to the fault and entirely localized in the footwall (right side; Fig. 5c).

5.2. Dipping fault models

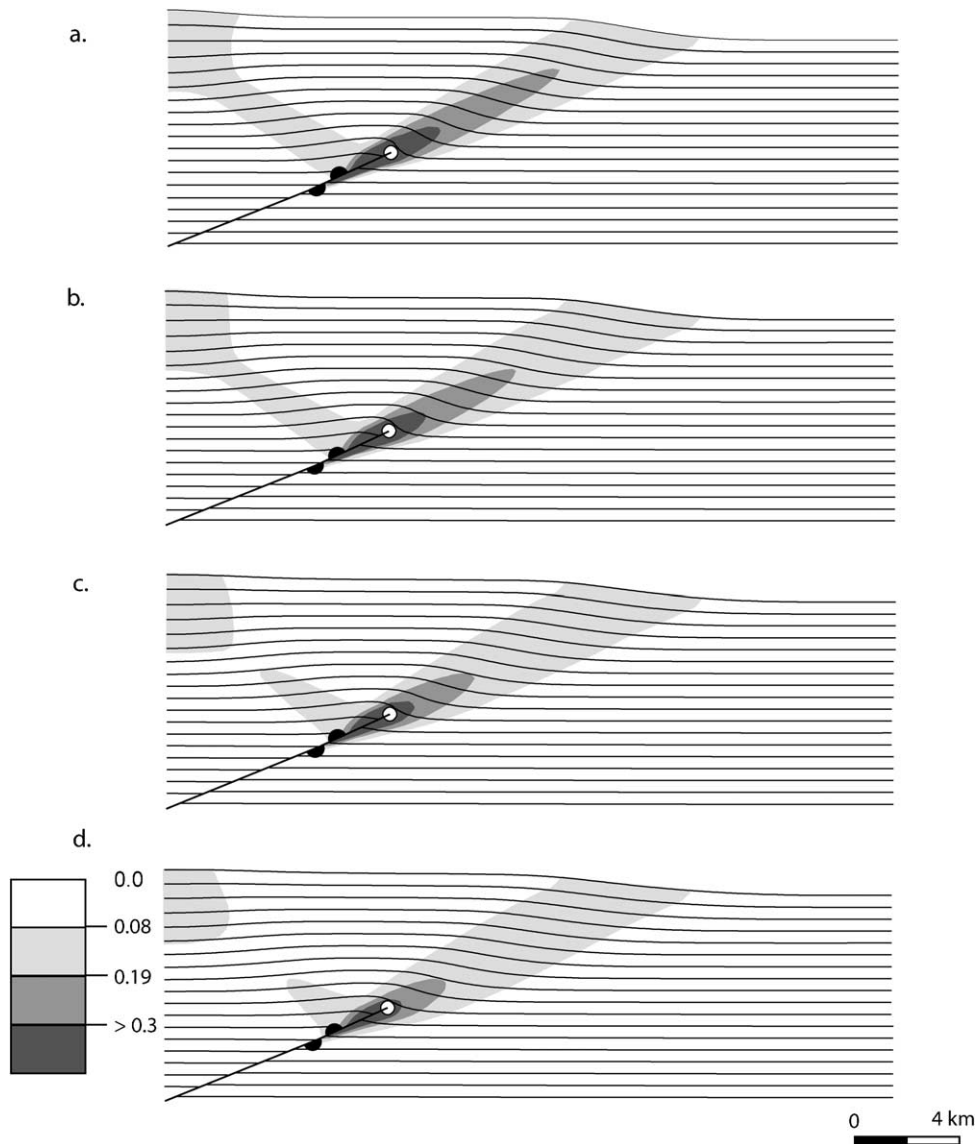A dipping fault propagating in a frictionless (Fig. 6a),

Fig. 9. Effects of material hardening on the fold geometry and the equivalent plastic strain generated by a dipping fault propagating in the compressible Drucker–Prager material. Strain hardening is specified by a hardening modulus of (a) −0.001 (strain softening), (b) 0.001, (c) 0.005, and (d) 0.01 the Young's modulus of the material.

frictional incompressible (Fig. 6b), or the frictional compressible (Fig. 6c) material, generates a symmetric (with respect to the fault) zone of plastic strain. The equivalent plastic strain in this zone increases towards the fault tip (Fig. 6). The resultant folds decrease in amplitude and increase in width away from the fault tip. The forelimbs taper from steep dips near the fault tip to more gentle dips at the surface (Fig. 6). However, there is an essential difference between folds formed in incompressible (Fig. 6a and b) and folds formed in the compressible material (Fig. 6c). In the compressible material, there is a conjugate band of plastic strain, and a gentle anticlinal backlimb (Fig. 6c). Such anticlinal backlimb has been observed in clay models (Groshong's model in Rodgers and Rizer, 1981), sandbox experiments (Mandl, 1988, his figure II.7-14), viscous

models (isotropic cover welded to the basement case of Johnson and Johnson, 2001), and particulate flow models (Finch et al., 2002).

Velocity fields derived by subtracting the displacements at the end and at 99% the total time of the experiments illustrate the kinematics of folding (left side; Fig. 7). In incompressible materials (left side; Fig. 7a and b) the velocity vectors are sub-parallel to the fault in the hanging wall, and decrease in magnitude but slightly in direction across a narrow triangular zone (with apex at the fault tip) symmetric to the fault. In the compressible material (left side; Fig. 7c) the velocity vectors rotate progressively upwards in the hanging wall, and change in magnitude but little in direction across a triangular zone ahead of the fault tip. Profiles of the velocities parallel and perpendicular to the fault (thick lines
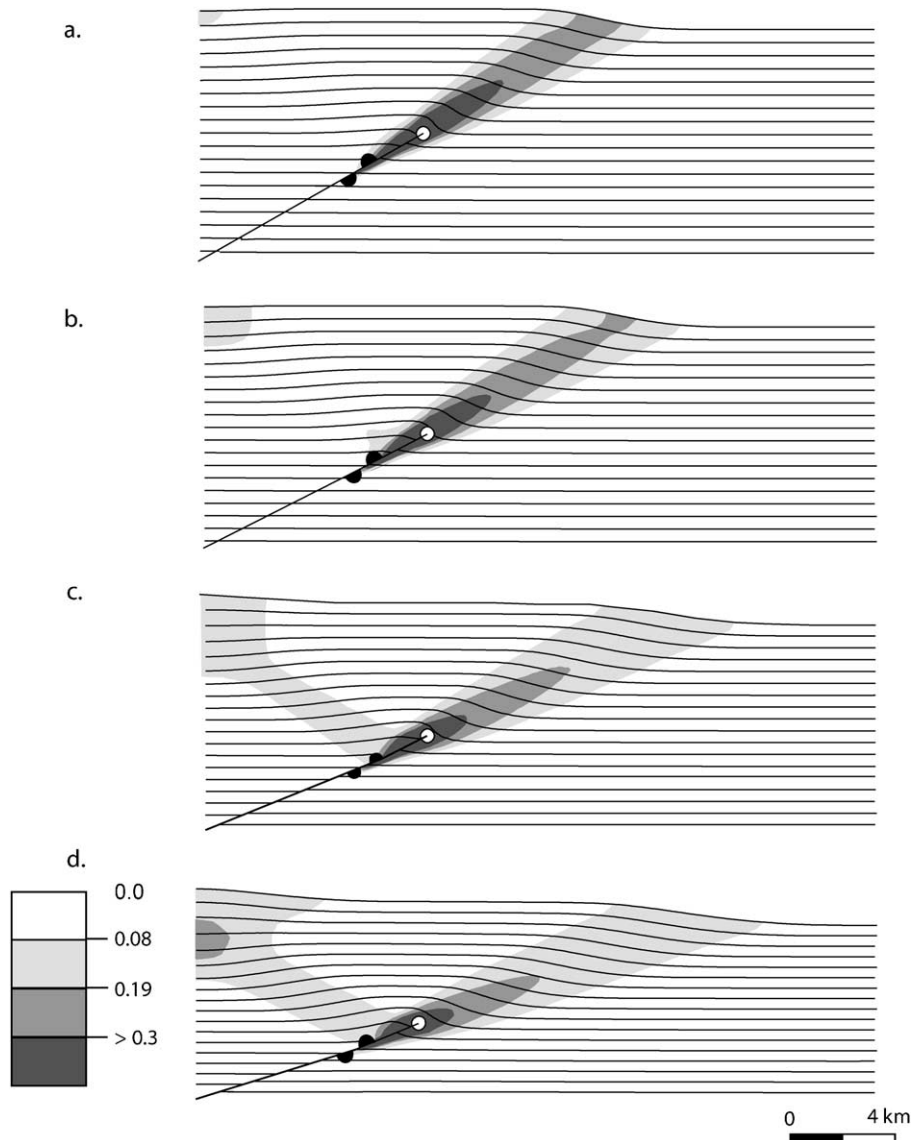
Fig. 10. Effects of material friction and dilation on the fold geometry and the equivalent plastic strain generated by a dipping fault propagating in the compressible Drucker–Prager material. Material friction and dilation angles are (a) 24, (b) 30, (c) 40, and (d) 46°. The corresponding Mohr–Coulomb friction angles are 15, 20, 30 and 40°, respectively.

on right side; Fig. 7) along a tie rod perpendicular to the fault and 2000 m ahead of the fault tip (heavy line on left side; Fig. 7) emphasize these observations. In incompressible materials, the velocity parallel to the fault decreases almost linearly across the triangular zone (thick continuous line on right side; Fig. 7a and b), while the velocity perpendicular to the fault slightly varies (thick dashed line on right side; Fig. 7a and b). These velocity profiles (thick lines on right side; Fig. 7a and b) are similar to those of the best-fit trishear models (thin lines on right side; Fig. 7a and b) for the fold geometries of the experiments (Fig. 6a and b). Like the mechanical experiments, the velocity parallel to the fault decreases linearly and the velocity perpendicular to the fault changes little across the triangular zone in the best-fit trishear models (thin lines; Fig. 7a and b). However, in the mechanical experiments the hanging wall also deforms

internally and moves slightly oblique to the fault (thick dashed line between 0 and 2 km, right side; Fig. 7a and b).

The velocity profiles of the compressible material (thick lines on right side; Fig. 7c) differ considerably from those of the best-fit trishear model (thin lines on right side; Fig. 7c) for the final geometry of the simulation (Fig. 6c). In the hanging wall, the velocity perpendicular to the fault (thick dashed line on right side; Fig. 7c) is almost 60% the velocity parallel to the fault (thick continuous line on right side; Fig. 7c). In front of the fault tip the velocities parallel and perpendicular to the fault decrease linearly (thick lines on right side; Fig. 7c), resulting in velocity vectors that change little in orientation (left side; Fig. 7c). The assumption of trishear (and of all kinematic models) of a rigid hanging wall moving parallel to the fault is obviously not justified in this simulation.
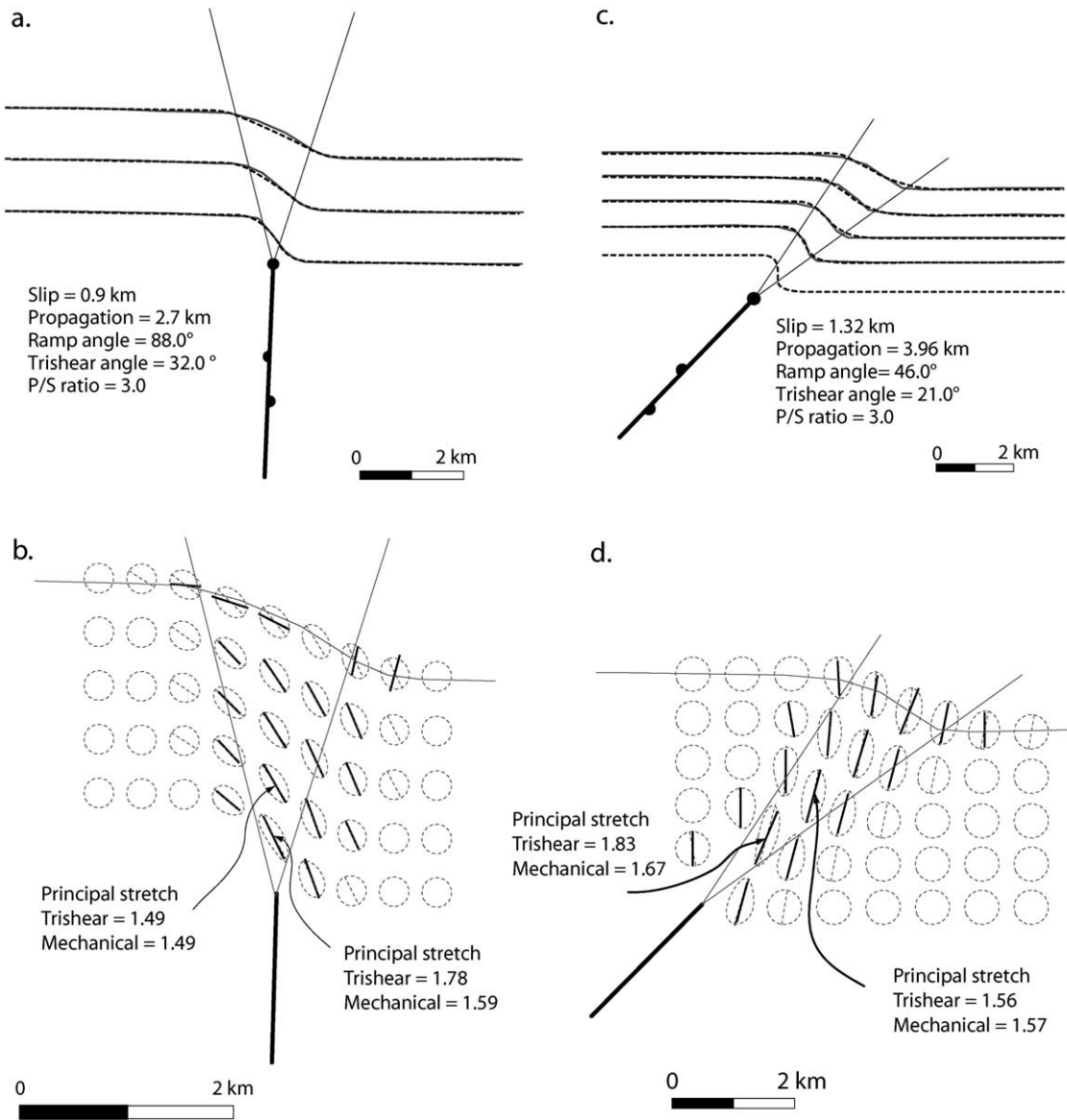
Fig. 11. Trishear modeling of the vertical (a and b) and dipping fault (c and d) experiments in incompressible frictionless materials. (a) and (c) Best fitting trishear models (dashed lines) superimposed on the final bed geometries of the mechanical simulations (continuous lines). (b) and (d) Strain ellipses and maximum principal strain axes of the best trishear models (dashed) superimposed on maximum principal strain axes of the mechanical simulations (thick lines). Note close coincidence in the orientation and the magnitude (i.e. length) of the axes of maximum principal strain. Stretch in the trishear model is averaged over the size of an initially unit diameter circle. Stretch in the mechanical model is a point wise value calculated at the center of the trishear ellipsoids.

5.3. Evolution of deformation

Contours of maximum principal strain rate superimposed on the deformed marker configuration at times 50, 75 and 100% the total time of the experiment, illustrate the evolution of the dipping fault simulation (Fig. 8). In frictionless (and similarly in frictional) incompressible materials, active yielding (indicated by the contours of maximum principal strain rate) occurs in a narrow zone slightly skewed towards the footwall (Fig. 8a). In the frictional compressible material active yielding occurs in two conjugate zones (Fig. 8b). In both cases, the zones of active yielding migrate with the fault tip (Fig. 8a and b). The fault propagates three times

faster than the material slips (Table 1), and therefore the material moves from the zone of active yielding ahead of the fault tip to the hanging wall (Fig. 8a and b; Allmendinger, 1998). The extent of the zones of active yielding decreases during the experiment. In frictionless incompressible materials at early stages, active yielding occurs from the initial fault tip location in the footwall to the surface (50%; Fig. 8a). Near the end of the experiment, active yielding occurs preferentially ahead of the fault tip (100%; Fig. 8a). In the frictional compressible material the extent of active yielding in the backlimb decreases during the simulation (Fig. 8b). Localization of strain rate towards the fault tip increases as the fault propagates in both simulations (Fig.

8a and b). The strain rate increases as the fault tip is approached like in the trishear model (Zehnder and Allmendinger, 2000).

The profiles of the velocities parallel and perpendicular to the fault change little during the experiments (Fig. 8c and d). In general, as the fault propagates the extent of the zone of velocity variation ahead of the fault tip slightly increases (compare profiles at the middle and at the end of the experiment; Fig. 8c and d). In frictionless incompressible materials, the internal deformation of the hanging wall outside the zone of velocity variation increases during the experiment (compare the velocity perpendicular to the fault at the middle and at the end of the experiment; Fig. 8c).

5.4. Varying material properties

We ran two sets of experiments in the frictional compressible material, one set varying material strain hardening (Fig. 9), and other set varying material friction and dilation angles (Fig. 10). The purpose of the experiments is to evaluate the effects of these material properties on the finite strain field of the resultant folds, especially in their backlimbs. Fig. 9 shows the equivalent plastic strain and final geometry produced by a dipping fault propagating in a strain softening material (Fig. 9a), or in a strain hardening material with a hardening modulus of 0.1 (Fig. 9b), 0.5 (Fig. 9c), and 1% (Fig. 9d) the material Young's modulus. Material strain hardening affects the finite strain field of the resultant structure. Increasing strain hardening produces folds that have lower equivalent plastic strains, lower fold amplitudes, and larger fold widths (Fig. 9a–d). These observations apply equally well to frictionless and frictional incompressible materials. In the backlimb, the extent of the conjugate plastic strain band, the magnitude of the equivalent plastic strain, and the amount of backlimb rotation, all decrease with increasing material strain hardening (Fig. 9a–d).

Fig. 10 illustrates the equivalent plastic strain and final geometry generated by a dipping fault propagating in the frictional compressible material with Drucker–Prager friction and dilation angles of 24 (Fig. 10a), 30 (Fig. 10b), 40 (Fig. 10c) and 46° (Fig. 10d). These values correspond to Mohr–Coulomb friction angles of 15, 20, 30 and 40° (Eqs. (1) and (2)). Increasing material friction and dilation angles decreases the equivalent plastic strain, the fold amplitudes, and increases the fold widths (Fig. 10a–d). Increasing material friction and dilation angles increases the extent of the backlimb plastic strain zone, the magnitude of the equivalent plastic strain in the backlimb, and the amount of backlimb rotation (Fig. 10a–d). Strain softening and dilation of the material ahead of the propagating fault tip enhance backlimb rotation.

5.5. Trishear modeling of the mechanical folds

The kinematics of fault propagation folding in elastoplastic incompressible materials is very similar to the kinematics of the trishear model. The mechanically generated fold geometries are trishear-like. One important question remaining is whether trishear can replicate the geometry and finite strain fields of the mechanical folds. Fig. 11 shows trishear modeling of folds generated by vertical and dipping faults propagating in frictionless incompressible materials. Forward trishear modelling using the best parameters from inverse modeling of the mechanical folds (Figs. 4a and 6a), produces geometries (dashed lines; Fig. 11a and c) that are remarkably close to those of the mechanical folds (continuous lines; Fig. 11a and c). The finite strain fields of the best-fit trishear models (dashed lines; Fig. 11b and d) are also very close in orientation and magnitude to the finite strain fields of the numerical models (represented by maximum principal strain axes, thick black lines; Fig. 11b and d). The orientation of the maximum principal strain axes and the amount of stretch along these axes in trishear and in the mechanical experiments are notably similar (Fig. 11b and d). Near the surface, however, there are differences in the geometries and strain fields of the two models, which are related to surface effects (Fig. 11). Trishear replicates the geometries and the finite strain fields of folds formed in frictionless incompressible materials.

6. Discussion

A fault propagating through an elastoplastic material produces a wave of deformation (i.e. yielding) in front of its tip line. This deformation is localized in a zone slightly asymmetric to the fault that migrates with the fault tip, and in an additional backlimb zone radiating from the fault tip in the case of the compressible material. Steady velocity fields characterize the deformation. In incompressible materials, the velocity vectors are slightly oblique to the fault and change in magnitude and orientation across a triangular zone symmetric to the fault. In the compressible material, the velocity vectors rotate progressively upward in the hanging wall and decrease linearly in magnitude but vary little in orientation across a triangular zone. Strain builds up as the fault propagates. The mechanical folds have forelimbs that taper from large dip angles near the fault tip to low dip angles at the surface, and in the case of the compressible material, gentle anticlinal backlimbs. Finite plastic strain is localized in a symmetric triangular zone, and in an additional backlimb zone in the compressible material.

The above description of fault propagation folding in elastoplastic materials has many similarities with trishear folding. In trishear a triangular zone of active shear migrates with the propagating fault tip. Folding in this zone is described by a steady velocity field that in its most basic formulation (a linear velocity field for a symmetric triangular zone) is remarkably similar to the velocity field exhibited by incompressible materials. Like the mechanical folds, trishear folds have forelimbs that taper up-section and finite strain fields localized in triangular zones symmetric to the fault, with strain magnitudes that increase towards the fault

tip. Trishear replicates remarkably well the geometry and the finite strain of the folds formed in incompressible materials. Regarding these materials, the configuration and the kinematics of trishear are thus mechanically reasonable, and the model succeeds in its purpose: reproducing finite strain.

None of the current kinematic models reproduces the progressive backlimb rotation and hanging wall uplift exhibited by the compressible material. One can argue that the compressible material with an associated flow rule ($\psi = \beta$), in which any increment of plastic shearing is accompanied by a proportional increase of volume (Mandl, 1988), is not a good representation of the brittle crust. It results in dilational strains of 60–100% close to the tip line and 10–20% in the backlimb; unrealistic values compared with the observed 10% dilational strain in deformation bands formed at low confining pressures in low porosity sandstones (Antonellini et al., 1994). Strayer and Hudleston (1997) suggested that non-associated plastic flow rules and incompressibility are indispensable to simulate the localization of deformation in the brittle crust. Nonetheless, incompressible materials fail to reproduce the observed dilation of rocks under shearing in the brittle range (Mandl, 1988; Morrow and Byerlee, 1989). The mechanical behavior of the upper brittle crust must be a compromise between the above two rheologies. The earth does not expand, but the brittle crust dilates during deformation. Backlimb rotation in compressible materials diminishes with progressive deformation (Fig. 8b), and increases with progressive material softening and dilation (Figs. 9 and 10). Backlimb rotation has been observed in analog and numerical models, and in field structures (e.g. Rip Van Winkle Anticline in the Hudson Valley fold-thrust belt; Marshak, 1990). We believe that under environmental conditions favorable to material dilation and strain softening, fault propagation folds with gentle anticlinal folds may form without a bend in the propagating fault, an idea almost heretical to the kinematic modeler.

The trishear grid search successfully predicts the *P/S* of the mechanical experiments. However our numerical models have one key limitation: the trajectory and the rate of fault propagation are prescribed. The models are unsuitable to explore the mechanical controls on *P/S*. One needs to develop models in which the fault propagates naturally in response to the loading conditions and the mechanical properties of the material. The trishear angles from inverse modeling of the mechanical folds are in a range of 20–30°, yet more open triangular zones (up to 100°) are observed in real structures (Allmendinger, 1998), in mechanical models of purely viscous materials (Johnson and Johnson, 2002), and in distinct element models (Finch et al., 2002). It is not clear under which mechanical conditions more diffuse zones of distributed shear can be produced in plastic materials and whether the kinematics in these zones is consistent with the trishear model. Increasing the yield stress and material strain hardening in elastoplastic materials slightly increases the apical angle of the

triangular zone (Fig. 9). But none of these material changes may produce the diffuse zones of plastic deformation observed in nature. Material anisotropy and heterogeneity, which are lacking in our experiments, may be essential in explaining such diffuse zones (Niño et al., 1998). Further research is needed to implement more realistic mechanical models with 'natural' fault tip propagation, and mechanical anisotropy.

References

Allmendinger, R.W., 1998. Inverse and forward numerical modeling of trishear fault-propagation folds. Tectonics 17, 640–656.

Allmendinger, R.W., Shaw, J.H., 2000. Estimation of fault propagation distance from fold shape; implications for earthquake hazard assessment. Geology 28, 1099–1102.

Allmendinger, R.W., Zapata, T.R., Manceda, R., Dzelalija, F., 2002. Trishear kinematic modeling of structures with examples from the Neuquén Basin, Argentina. Thrust Tectonics Conference. American Association of Petroleum Geologists, Special Publication, in press.

Antonellini, M.A., Aydin, A., Pollard, D.D., 1994. Microstructure of deformation bands in porous sandstones at Arches National Park, Utah. Journal of Structural Geology 16, 941–959.

Berg, R.R., 1962. Mountain flank thrusting in Rocky Mountain foreland, Wyoming and Colorado. American Association of Petroleum Geologists Bulletin 46, 2019–2032.

Bird, P., Baumgardner, J., 1984. Fault friction, regional stress, and crust–mantle coupling in southern California from finite element models. Journal of Geophysical Research 89, 1932–1944.

Braun, J., Sambridge, M., 1994. Dynamical Lagrangian Remeshing (DLR): a new algorithm for solving large strain deformation problems and its application to fault-propagation folding. Earth and Planetary Science Letters 124, 211–220.

Byerlee, J.D., 1978. Friction of rocks. Pure and Applied Geophysics 116, 615–626.

Carmichael, R.S., 1989. Practical Handbook of Physical Properties of Rocks and Minerals. CRC Press, Boca Raton.

Chen, Y., Lin, Z., Lin, B., Li, Z., 1978. The focal mechanism of the 1966 Xingtai earthquake as inferred from ground deformation observations. Chinese Geophysics 1, 263–288.

Desai, C.S., Siriwardane, H.J., 1984. Constitutive Laws for Engineering Materials with Emphasis on Geologic Materials. Prentice-Hall, Engelwood Cliffs.

Elliott, D., 1976. The motion of thrust sheets. Journal of Geophysical Research 81, 949–963.

Erslev, E.A., 1991. Trishear fault-propagation folding. Geology 19, 617–620.

Finch, E., Hardy, S., Gawthorpe, R., 2002. Discrete element modeling of compressional fault propagation folding above rigid basement fault blocks. Journal of Structural Geology in press.

Gregg Erickson, S., Jamison, W.R., 1995. Viscous–plastic finite-element models of fault-bend folds. Journal of Structural Geology 17, 561–573.

Hardy, S., Ford, M., 1997. Numerical modeling of trishear fault propagation folding. Tectonics 16 (5), 841–854.

Hill, R., 1950. The Mathematical Theory of Plasticity. Oxford University Press, London.

Hoek, E., 2000. Practical Rock Engineering. http://www.rockeng.utoronto.ca/roc/Hoek/Hoeknotes2000.htm.

Hubbert, M.K., 1951. Mechanical basis for certain familiar geological structures. Bulletin Geological Society of America 62, 355–372.

Jaeger, J.D., Cook, W., 1979. Fundamentals of Rock Mechanics. Chapman and Hall, London.

Johnson, A.M., 2001. The Purdue Faux Pli Manual, vol. 1. Purdue Research Foundation, Purdue University. http://www.eas.purdue.edu/fauxpli.

Johnson, A.M., Fletcher, R.C., 1994. Folding of Viscous Layers; Mechanical Analysis and Interpretation of Structures in Deformed Rock. Columbia University Press, New York.

Johnson, K.M., Johnson, A.M., 2001. Volume 5: Mechanical analysis of the geometry of forced-folds. In: The Purdue Faux Pli Manual, Purdue Research Foundation, Purdue University. http://www.eas.purdue.edu/fauxpli.

Johnson, K.M., Johnson, A.M., 2002. Mechanical models of Trishear-like folds. Journal of Structural Geology 24, 277–287.

King, G.C.P., Stein, R.S., Brundle, J.B., 1988. The growth of geological structures by repeated earthquakes. 1. Conceptual framework. Journal of Geophysical Research 93, 13307–13318.

Kulhawy, F.H., 1973. Analysis of underground openings in rock by finite element methods. Final report/U.S. Bureau of Mines. Dept. of Civil Engineering, Syracuse University.

Livesey, G.B., 1985. Laramide structures of southeastern Sand Wash Basin. In: Gries, R.R., Dyer, R.C. (Eds.). Seismic Exploration of the Rocky Mountain Region. Rocky Mountain Association of Geologists, Denver, pp. 87–94.

Mandl, G., 1988. Mechanics of Tectonic Faulting. Models and Basic Concepts. Elsevier Science Publishers, Amsterdam, Netherlands.

Manshinha, L., Smylie, D.E., 1971. The displacement fields of inclined faults. Bulletin Seismological Society of America 61, 1433–1440.

Marshak, S., 1990. Structural Geology of Silurian and Devonian Strata in the Mid-Hudson Valley, New York: Fold–Thrust Belt Tectonics in Miniature. Geological Survey, New York State Museum, Map and Chart Series 41.

Mendelson, A., 1968. Plasticity, Theory and Application. Macmillan, New York.

Morrow, C.A., Byerlee, J.D., 1989. Experimental studies of compaction and dilatancy during frictional sliding on faults containing gouge. Journal of Structural Geology 11, 815–825.

Niño, F., Philip, H., Chéry, J., 1998. The role of bed-parallel slip in the formation of blind thrust faults. Journal of Structural Geology 20, 503–516.

Patton, T.L., Fletcher, R.C., 1995. Mathematical block-motion model for deformation of a layer above a buried fault of arbitrary dip and sense of slip. Journal of Structural Geology 17, 1455–1472.

Pollard, D.D., Segall, P., 1987. Theoretical displacements and stresses near fractures in rock: with applications to faults, joints, veins, dikes, and solution surfaces. In: Atkinson, B.K. (Ed.). Fracture Mechanics of Rock. Academic, San Diego, CA, pp. 277–349.

Prucha, J.J., Graham, J.A., Nickelsen, R.P., 1965. Basement-controlled deformation in Wyoming province of Rocky Mountain foreland. American Association of Petroleum Geologists 49, 966–992.

Ranalli, G., 1987. Rheology of the Earth: Deformation and Flow Processes in Geophysics and Geodynamics. Allen and Unwin Inc, Boston.

Rice, J.R., 1968. Mathematical analysis in the mechanics of fracture. In: Liebowitz, H. (Ed.). Fracture. An Advanced Treatise. Academic Press, New York, pp. 192–311.

Rodgers, D.A., Rizer, W.D., 1981. Deformation and secondary faulting near the leading edge of a thrust fault. In: McClay, K.R., Price, N.J. (Eds.). Thrust and Nappe Tectonics. Geological Society of London, pp. 65–77.

Sanford, A.R., 1959. Analytical and experimental study of simple geologic structures. Bulletin Geological Society of America 70, 19–52.

Savage, J.C., Hastie, L.M., 1969. A dislocation model for the Fairview Peak, Nevada, Earthquake. Bulletin Seismological Society of America 59, 1937–1948.

Smart, K.J., Krieg, R.D., Dunne, W.M., 1999. Deformation behavior during blind thrust translation as a function of fault strength. Journal of Structural Geology 21 (7), 855–874.

Stearns, D.W., 1971. Mechanisms of drape folding in the Wyoming province. In: Wyoming Geological Association 23rd Annual Field Conference Guidebook, pp. 125–143.

Stearns, D.W., 1978. Faulting and forced folding in the Rocky Mountain foreland. Geological Society of America Memoir 151, 1–38.

Strayer, L.M., Hudleston, P.J., 1997. Numerical modeling of fold initiation at thrust ramps. Journal of Structural Geology 19, 551–566.

Suppe, J., 1985. Principles of Structural Geology. Prentice Hall, Englewood Cliffs, NJ.

Suppe, J., Medwedeff, D.A., 1990. Geometry and kinematics of fault-propagation folding. Eclogae Geologicae Helvetiae 83, 409–454.

Turcotte, D.L., Schubert, G., 1982. Geodynamics: Applications of Continuum Physics to Geological Problems. John Wiley and Sons, New York.

Williams, G., Chapman, T., 1983. Strains developed in the hanging walls of thrusts due to their slip/propagation rate: a dislocation model. Journal of Structural Geology 5, 563–571.

Yeats, R.S., Huftile, G.J., 1995. The Oak Ridge fault system and the 1994 Northridge earthquake. Nature 373, 418–420.

Zehnder, A.T., Allmendinger, R.W., 2000. Velocity field for the trishear model. Journal of Structural Geology 22, 1009–1014.